Model-based validation of a tracking algorithm to quantify strain in muscles from two-dimensional ultrasound images

by

J. de Graaf

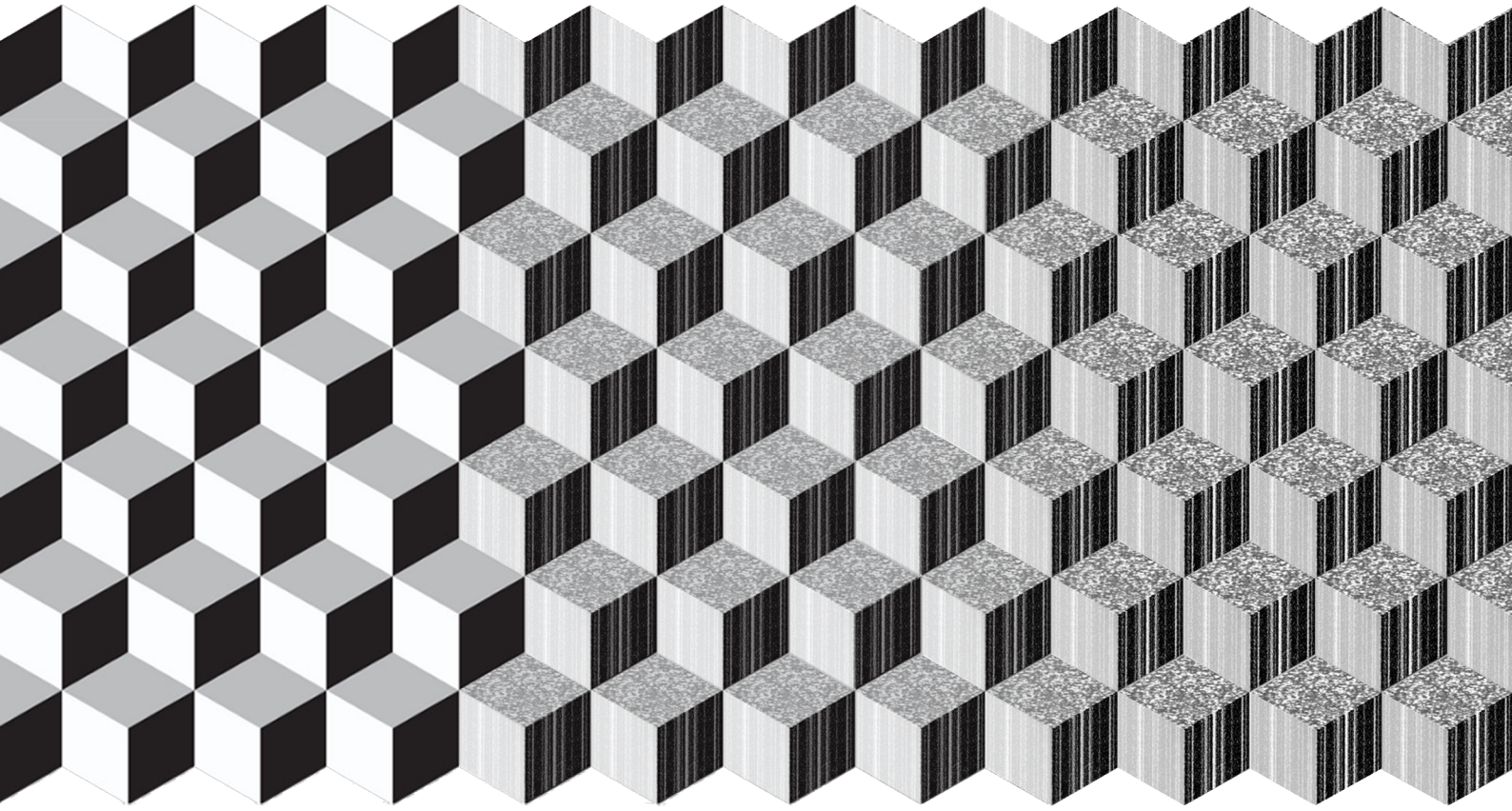

to obtain the degree of Master of Science
at the Delft University of Technology,
to be defended publicly on Wednesday April 17, 2019 at 10:00 AM.

Student number: 4108582
Project duration: October, 2018 – April, 2019
Thesis committee:

Dr. ir. A.C. Schouten	TU Delft, chairman
Dr. ir. W. Mugge	TU Delft
Ir. C. Kasbergen	TU Delft
Dr. H. Maas	VU
Prof. dr. R.D Herbert	NeuRA
Dr. ir. B. Bolsterlee	NeuRA, daily supervisor

TU Delft

Model-based validation of a tracking algorithm to quantify strain in muscles from two-dimensional ultrasound images

Jurjan de Graaf

Delft University of Technology

Abstract

Fascicle shear is theoretically a mechanism by which skeletal muscles lengthen. Existing ultrasound based techniques allow measurement of muscle architecture parameters, but not the quantification of shear strain. In this study, an algorithm that tracks the shear strain from ultrasound images using a continuum representation of the muscle was developed. Errors in strain tracking may arise due to misalignment of the imaging plane, movement artifacts and non-uniform strain within the muscle. The goal of this study was to develop and validate the newly developed strain tracking algorithm. Various potential sources of error are investigated.

A computer model was created consisting of a three-dimensional (3D) synthetic volume, representing the muscle. Virtual ultrasound images were then sampled from the 3D volume by intersecting the synthetic volume under a known angle of the imaging plane. The measurement error was defined as the difference between the known strain that was imposed virtually to the 3D muscle volume and the strain calculated with the tracking algorithm. The measurement error was determined for conditions of combined axial and shear strain, plane misalignment, plane rotation and non-uniform strain. Conditions were simulated between 30 and 100 times, each time with a different synthetic muscle volume.

The developed strain tracking algorithm provided strain measurement of sub-pixel accuracy and precision when the imaging plane was aligned with the fascicles. Rotation of the ultrasound transducer relative to the muscle resulted in invalid measurements. Axial strain was overestimated when the muscle exhibited a non-uniform axial strain pattern. Largest errors (underestimation of strain by up to 65%) were caused by misalignment of the imaging plane with the fascicles. The large effect of misalignment emphasizes the need for careful transducer placement that requires anatomical information about the muscle structure. Strain tracking methods based on three-dimensional avoid the need for alignment, potentially allowing more accurate measurement of strain.

1. Introduction

In human movement, joint rotation is facilitated through a length change of the muscle belly and the tendon. Lengthening of the muscle belly is facilitated through several mechanisms. Elongation of fascicles, a change in pennation angle and a change in fascicle curvature are able to contribute to lengthening (Azizi et al., 2008, Bolsterlee et al., 2017). A less obvious, potential mechanism for the muscle belly to lengthen, is through shear deformation (Herbert et al., 2018). Shear of the muscle belly in the fascicle direction, could cause the muscle belly to lengthen without elongation of muscle fascicles. It is not yet known if fascicle shear actually contributes to lengthening of the human muscle belly.

Fascicle shear plays an important role in the transmission of length and force in the muscle. It is long known that the muscle is able to transmit shear loads effectively (Street, 1983, Purslow and Trotter, 1994, Huijing, 1999, Sharafi et al., 2011). Alterations in shear stiffness of the muscle have been linked to neuromuscular disease, aging, and a reduction in force producing capacity (Eby et al., 2015, Lee et al., 2016, Jakubowski et al., 2017). However, the contribution of shear strain to length

Email address: jurjandegraaf@gmail.com (Jurjan de Graaf)

change of the muscle has only recently been proposed (Herbert et al., 2018). A model of pennate muscle predicted that fascicle shear strain could theoretically contribute as much to length change as axial strains of fascicles. Shear straining of fascicles could occur independently from changes in pennation (Blemker et al., 2005). To better understand the role of shear strain in lengthening of the muscle, characterization of the strain patterns *in-vivo* is needed.

Strain patterns and muscle architecture are widely studied using ultrasound and MRI imaging techniques. MRI has a higher spatial resolution, but ultrasound has a higher temporal resolution. Consequently, ultrasound allows analysis of the muscle during dynamic conditions, such as lengthening and shortening, but typically provides two-dimensional images. Applications of imaging techniques include the study of muscle architecture under different conditions. Many pathological conditions of the muscle, such as contracture, are manifested through alterations in the muscle architecture (Hoang et al., 2009, Barber et al., 2011, Kwah et al., 2012). Alterations in fascicle length, pennation angle and fascicle curvature can be tracked in a sequence of ultrasound images using automated open source software (Farris et al., 2016). However, a method to measure the shear strain from 2D ultrasound images of skeletal muscle is not available.

An algorithm that quantifies strain in the muscle from 2D ultrasound imaging was developed in the present study. By tracking features in a sequence of images, a method referred to as digital image correlation (DIC), displacement fields can be estimated (Pan et al., 2009, Boyle et al., 2014). In this study, the integration of DIC with the estimation of strain is also referred to as strain tracking. Strain tracking can be applied to existing ultrasound videos that were used to measure muscle architecture. Concerns may be raised for the estimation of strain and the validity of DIC. Therefore, potential sources of measurement errors should be investigated.

The primary goal of present study is to validate strain tracking in skeletal muscle from 2D ultrasound images. Development of the strain tracking algorithm is the secondary goal of this study, and necessary for the validation. Strain tracking is expected to have similar accuracy and precision to that of other applications based on DIC, for example the quantification of strain in rat tendon or human vertebra (Okotie et al., 2012, Boyle et al., 2014, Palanca et al., 2015). Scenarios, specific to ultrasound imaging of the muscle should be investigated as well. A muscle changes shape in three dimensions when it changes length or activates, but ultrasound imaging only captures two dimensions of the deformations. Errors in muscle architecture measurements are introduced if the imaging plane is misaligned with the fascicle (Klimstra et al., 2007, Bénard et al., 2009, Kellis et al., 2009, Bolsterlee et al., 2016). It is hypothesized that plane misalignment causes underestimation of fascicle strain as measured by the algorithm; the fascicle strain in the 2D imaging plane is measured, which may only be a fraction of the fascicle strain that occurs in the 3D muscle. Furthermore, the relative movement of the ultrasound probe with respect to the muscle may lead to the imaging of different structures and false tracking of features, resulting in measurement errors referred to as movement artifacts. The sensitivity of movement artifacts to the relative movement of the imaging plane with the muscle will be investigated. It is expected that the tracking algorithm is able to reliable distinguish features, and movement artifacts will not cause a substantial error. Finally, large non-uniformities of strain in the muscle under physiological conditions have been reported (Blemker et al., 2005, Shin et al., 2009, Englund et al., 2011). The hypothesis is that non-uniform strain results into measurement errors of the algorithm. Therefore, the sensitivity of the measurement error due to non-uniform strain patterns will be explored.

The deformation of the muscle will be determined from B-mode ultrasound imaging using DIC. From the deformation, axial and shear strain in the fiber direction will be calculated using a continuum approach (Criscione et al., 2001, Blemker et al., 2005). The strain tracking algorithm will be applied to virtual ultrasound images generated from an imaging plane that intersects with a 3D virtual model of the muscle. The measurement error will be defined as the difference between the strain imposed to the 3D muscle volume and the strain calculated with the tracking algorithm. The imposed strain on the 3D muscle model and movement of the imaging plane will be varied to investigate the measurement error for conditions of combined axial and shear strain, plane misalignment, plane rotation and non-uniform strain in the muscle.

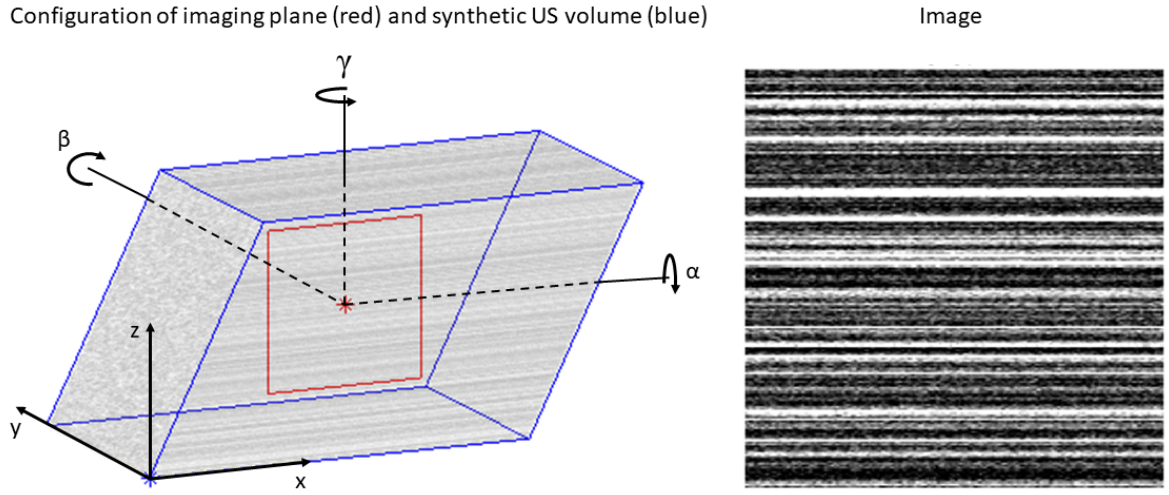

Figure 1. To the left, the location and shape of the imaging plane (red) and the synthetic volume (blue) are shown. The general coordinate system and the angles for rotation of the imaging plane are depicted. The synthetic volume is made translucent and has been deformed from its original cuboid shape. A shear strain of 50% has been applied ($\epsilon_{xz} = 0.5$) To the right, the ultrasound image that corresponds to the configuration is shown. Fascicles are horizontal striations because the imaging plane is aligned with the fascicle direction.

2. Methods

2.1. Virtual ultrasound images

Two-dimensional (2D) ultrasound images were obtained by slicing a plane through a synthetic 3D ultrasound volume. The plane is referred to as the imaging plane and the synthetic ultrasound volume represents the muscle. Figure 1 shows a configuration of the imaging plane and synthetic volume with the corresponding image. The synthetic volume is generated from a 3D matrix, each entry corresponding to a voxel with a grayscale value between zero (black) and one (white). Grayscale values of the synthetic volume are linearly interpolated over the location of the imaging plane to form an image. By generating a consecutive number of images, a virtual ultrasound video can be created. The number of frames of the video is determined by the amount of simulation steps.

2.1.1. Synthetic ultrasound volumes

A program was written for the generation of the synthetic ultrasound volume. Generation of the synthetic volume is a random process; fascicle location, fascicle geometry and speckle pattern were randomly assigned, resulting in a unique synthetic volume for every run of the program. Figure 2 shows two synthetic volumes that have been generated using the same parameters. Unidirectional bright lines within the volume represent the fascicles. The fascicles vary in radius and are randomly spaced.

Fascicles were created by generating their cross section in a plane. In Fig 2, the cross sectional plane is the yz-plane and the fascicles run in the x-direction. The location of the fascicle centers were randomly assigned in the cross sectional plane. The number of fascicle centers generated in the yz-plane was given by the areal density parameter ρ_{fib}. The fascicles have a thickness that was modelled as a gradient of the brightness. The brightness decreases linearly from the fascicle center to the fascicle radius r_{fib}. The starting value of the brightness gradient was drawn from a uniform distribution on the interval between c_{low} and c_{high}. Consequently, variability in brightness of the fascicles was introduced. Additionally, variability of fascicle thickness was modelled by drawing r_{fib} from a normal distribution with mean $\mu_{r_{fib}}$ and standard deviation $\sigma_{r_{fib}}$. After generation of the cross sectional plane, the final step was duplication in the fascicle direction to create a 3D volume. An example of a generated volume, which resembles the appearance of skeletal muscle on ultrasound images, is shown in the left of Figure 2.

To simulate the granular appearance of US imaging, a speckle pattern was added to the synthetic 3D volume. The speckle pattern was modelled as a nor-

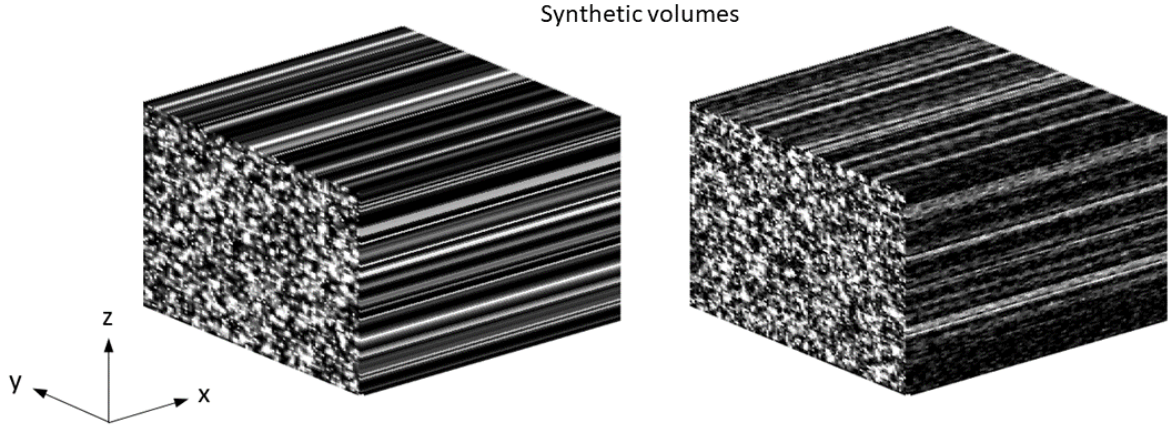

Figure 2. Two different synthetic volumes of 100x100x100 voxels are shown. The left is without a granular speckle pattern and shows the geometry of the fascicles. The cross section of the fascicles in the yz plane was duplicated in fascicle direction along the x axis. To the right, a synthetic volume with a speckle pattern is shown that resembles the volumes used for simulations. Apart from the speckle pattern, both data sets were generated using the same parameters (Example in Table I).

mally distributed deviation σ_{gran} of the grayscale value of each voxel. The speckle pattern introduces contrast on the voxel level that enhances tracking of the voxels. Figure 2 shows two generated volumes, the left one with and the right one without a speckle pattern.

Parameters for generation of the synthetic volume were chosen by trial and error. Parameters were chosen so that the virtual images roughly resembled 2D ultrasound imaging of the gastrocnemius (see Appendix A). The chosen parameters are presented in Table I.

Table I. Table of the parameters used for the generation of the synthetic volumes.

Synthetic volume generation parameter	Symbol	Value
Fascicle areal density	ρ_{fib}	0.4 fascicle/voxel^2
Interval uniform distribution of starting value fascicle brightness	$c_{low} - c_{high}$	0 - 0.4 grayscale value
fascicle radii (Mean + SD)	$\mu_{r_{fib}} \pm \sigma_{r_{fib}}$	1.5 ± 0.5 voxel
Speckle generation noise SD	σ_{gran}	1/6 grayscale value

2.1.2. Transformations of the synthetic volume and the imaging plane

Different transformations can be imposed to the synthetic volume and imaging plane. The imaging plane may be specified to rotate. Rotation of the imaging plane around its local x,y and z axis correspond to the angles α,β and γ (Figure 1). The angle α and γ correspond to the convention of tilt and rotation as used in previous studies (Bénard et al., 2009, Bolsterlee et al., 2016). For the goals of this study, we only performed simulations where the angle γ (rotation) were varied.

In addition to rotation of the imaging plane, the synthetic volume may also deform. Uniform or non-uniform deformations can be imposed to the synthetic volume. In case of uniform deformation, the applied strain is linear. The strain tensor $\boldsymbol{\epsilon}$ corresponding to linear deformation in 3D is given by the following expression:

$$\boldsymbol{\epsilon} = \begin{bmatrix} \epsilon_{xx} & \epsilon_{xy} & \epsilon_{xz} \\ \epsilon_{yx} & \epsilon_{yy} & \epsilon_{yz} \\ \epsilon_{zx} & \epsilon_{zy} & \epsilon_{zz} \end{bmatrix} \quad (1)$$

Here the diagonal elements ϵ_{xx}, ϵ_{xy}, and ϵ_{xz} represent the axial strains in the x, y, and z direction respectively. The off diagonal elements, ϵ_{xy}, ϵ_{xz} and ϵ_{yx}, ϵ_{yz} and ϵ_{zx}, ϵ_{zy} represent the shear strains in the xy, xz, and yz planes respectively.

For the goals of this study, only two directions of strain were applied; axial strain in the fascicle direction ϵ_{xx}, and shear strain in the ϵ_{xz} plane along the fascicle direction. These directions of strain in the xz-plane are aligned with the imaging plane when α, β and γ are zero (the neutral orientation of the plane). In case non-uniform deformation was imposed, a deformation field was specified. Only one case of non-uniform deformation was used in this study; axial strain that increases linearly along the fascicle direction with increment $\Delta\epsilon_{xx}$.

2.2. Strain tracker

An algorithm for the measurement of strain in the muscle from ultrasound videos was developed. The algorithm is referred to as strain tracker. The strain tracker follows features (also called speckles) in consecutive video frames, estimates the geometric transformation of the muscle and calculates the corresponding strain. The strain tracker was developed in MATLAB and exploits algorithms from the computer vision system toolbox (MATLAB 2017B, The MathWorks).

The strain tracker starts with the processing of the first video frame. A region of interest (ROI) within the muscle is selected by the user. The ROI is subdivided into a number of square boxes predefined by the user. Each box is aligned with the fascicle orientation. The fascicle orientation is automatically determined using Canny edge detection and the Radon transform. In this study, the ROI is subdivided into one box only. Within the box, the minimum eigenvalue algorithm detects the points most suitable for tracking (Shi and Tomasi, 1994). Points suitable for tracking are found in areas where neighboring pixels have a high contrast. Figure 3 shows an example of a first video frame including the box and the set of points most suited for tracking.

The following step is the tracking of points and estimation of the geometric transformation. The Kanade-Lucas-Tomasi (KLT) algorithm is used to track points from the current video frame to the next video frame (Tomasi et al., 1991). This leads to two sets of points that correspond to the same observed features. The transformation T that maps the current set of points to the next set of points is estimated using the M-estimator SAmple and Consensus (MSAC) algorithm (Torr and Zisserman, 2000). The MSAC algorithm estimates one best fit transformation that maps most of the points. The estimated transformation T is assumed to be affine. Figure 3 shows the box encompassing the tracked points before and after the volume is transformed.

Some points cannot be tracked reliably between subsequent frames because of two reasons. First, the KLT algorithm is unable to find the same point in the follow up frame. Second, the point in the follow up frame lies too far from its location estimated by the transformation T; the point is an outlier and it is omitted. The amount of lost points is influenced by the settings of the algorithms. Settings of the algorithms were determined by trial and error. The settings remained constant for all simulations and are reported in Table II.

Table II. Table enlisting the settings of the strain tracker. The same settings were used for all simulations

Strain tracker setting	value
Size of box in ROI	100x100 pixel
Block size (KLT)	31 pixel
Maximum bidirectional error (KLT)	2 pixel
Maximum pixel distance (MSAC)	2 pixel

2.2.1. Calculation of Strain

Strain was calculated under the assumption that the muscle is a continuous fibre-reinforced composite. The fibres of the composite are represented by the fascicles. The strain was calculated based on the estimated transformation T. From the transformation, the translational part was removed to obtain the two-dimensional deformation gradient F. Using the deformation gradient F, the right Cauchy Green tensor C was calculated.

$$C = F^T F \tag{2}$$

Strain invariants from C were used to represent components of strain in a material frame of reference that was aligned with the fiber orientation. The strain invariants allow calculation of the fibre strain ϵ_M and the along fibre shear strain ϵ_D. Strain invariants derived for a transversely isotropic material in 3D were adopted for the current 2D case (Criscione et al., 2001). Two strain invariants were used; the fibre stretch λ_M and the component of the simple shear in the fibre direction Ψ. The fibre stretch λ_M is described as follows:

$$\lambda_M = \sqrt{M \cdot CM} \tag{3}$$

where M denotes the unit vector in the fibre direction. The small strain in the fiber direction ϵ_M is calculated as the fibre stretch λ_M minus one:

$$\epsilon_M = \lambda_M - 1 \tag{4}$$

The strain invariant Ψ expresses the ratio of the along fibre shear strain ϵ_D to the fibre stretch λ_M (Blemker et al., 2005). The strain invariant Ψ is calculated as:

$$\Psi = \frac{\epsilon_D}{\lambda_M} = \sqrt{\frac{M \cdot C^2 M - (M \cdot CM)^2}{M \cdot CM}} \tag{5}$$

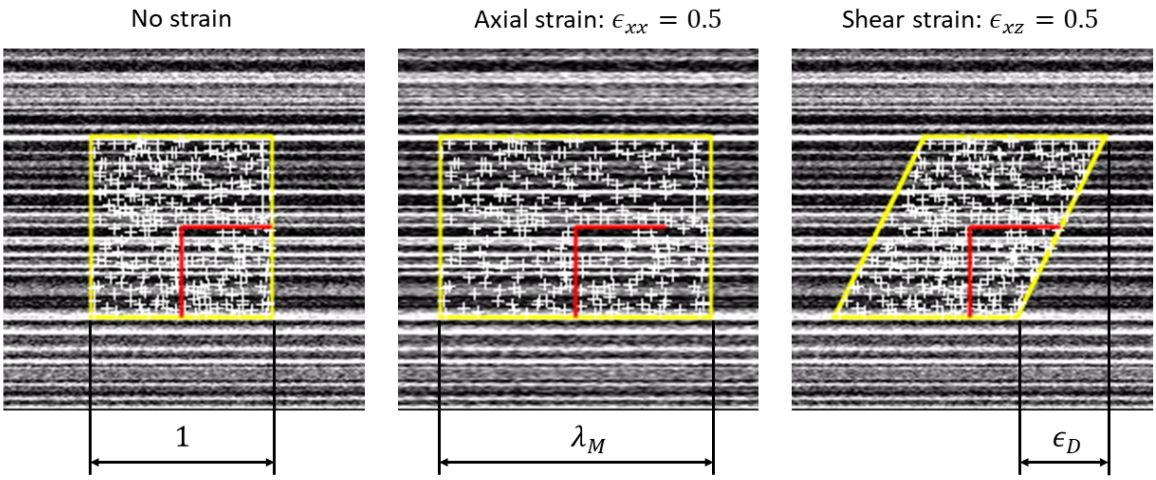

Figure 3. Three tracked frames are shown. The left shows the initial configuration in the first video frame. The yellow box encloses the region that is tracked. The white crosses mark the points that are being tracked. Strains are normalized to dimensions of the box in the first frame. The fascicle direction is marked by the red horizontal line. The two red lines form the local axis system of the tracked region (positive x to the right, positive y downward). In the middle, a frame showing 50% axial strain is depicted. The corresponding fibre stretch is $\lambda_M = 1.5$. To the right, a shear strain of 50% in the xz plane is depicted. This frame could have been the result of the configuration of the synthetic volume and imaging plane shown in Figure 1.

Multiplying Ψ with the fibre stretch λ_M yields the along fiber shear strain ϵ_D:

$$\epsilon_D = \lambda_M \Psi \tag{6}$$

The resulting definitions for the fibre strain ϵ_M and along fibre shear ϵ_D were used in the strain tracker (Figure 3).

2.3. Validation experiments

Four conditions were simulated to assess validity and performance of the strain tracker. In each simulation, a range of conditions was assessed. Each condition was repeated at least 30 runs, each run with a different synthetic volume. An overview of the simulations is given in Table III.

Performance of the strain tracker was assessed by two measures. First, the strain estimation was evaluated by comparing the imposed strain (true strain) to the strain measured by the strain tracker (measured strain). The difference between the true strain and measured strain is the error. The relative error was defined as the fraction of the error over the true strain, in percentage. Second, performance of the point tracker (KLT) was assessed by evaluating the fraction of lost points. The fraction of lost points describes the amount of features that are not recognized in the current frame, with respect to the first frame.

Table III. A description of the simulations and the corresponding conditions. Every condition consists of two or more image frames, and was repeated a number of runs. For every run, new synthetic data was generated.

#	Simulation description	Conditions	Runs / condition	Frames / condition
1	Combined axial and shear strain	1. $\epsilon_{xx} = 0.2\%$, $\epsilon_{xz} = 0.2\%$ 2. $\epsilon_{xx} = 2\%$, $\epsilon_{xz} = 2\%$ 3. $\epsilon_{xx} = 20\%$, $\epsilon_{xz} = 20\%$	100	2
2	Strain while imaging plane is misaligned	1. $\gamma = 0^\circ$ 2. $\gamma = 1^\circ$: 11. $\gamma = 10^\circ$ All conditions: $\epsilon_{xx} = 2\%$, $\epsilon_{xz} = 2\%$	30	2
3	Rotational velocity of imaging plane, no strain	1. $\dot{\gamma} = 0.1^\circ$/frame 2. $\dot{\gamma} = 0.2^\circ$/frame : 8. $\dot{\gamma} = 0.8^\circ$/frame	30	1. 41 2. 21 : 8. 6
4	Non-uniform strain; linearly increasing axial strain	1. $\Delta\epsilon_{xx} = 0.04\%$/voxel 2. $\Delta\epsilon_{xx} = 0.08\%$/voxel : 10. $\Delta\epsilon_{xx} = 0.40\%$/voxel	30	2

The first simulation evaluates the accuracy and precision of the strain tracker (examples in Appendix B). Additionally, the ability of the tracker to distinguish axial strain from shear strain was determined. To achieve this, three combinations of axial strain ϵ_{xx} and shear strain ϵ_{xz} were applied. The axial and shear strain both ranged from 0.2% to 20%.

In the second simulation, the effect of imaging

plane misalignment on strain measurement error was evaluated. This was examined by setting the imaging plane under various angles γ while strain was applied to the volume. The angle γ ranged from 0 to 10 degrees which reflects the range of imaging plane misalignment with fascicles found in previous studies (Bolsterlee et al., 2015, Bénard et al., 2009).

The third simulation investigated whether a rotation of the imaging plane with velocity $\dot{\gamma}$ could lead to measurement of strain. The plane started aligned with fascicles and rotated with an angular velocity $\dot{\gamma}$. This resulted into gradual plane misalignment and fascicle sections within the 2D image becoming shorter ((Bolsterlee et al., 2016), Appendix C). However, the fascicles did not actually shorten since no strain was applied to the synthetic volume. The angular velocity $\dot{\gamma}$ ranged from 0.1°per frame to 0.8° per frame. The number of frames ranged from 6 to 41 frames to obtain a final angular displacement γ of at least 4.0 degrees.

The fourth simulation demonstrated the effect of non-uniform strain on tracking performance. A strain that increased linearly with increment $\Delta\epsilon_{xx}$ along the fascicle direction (x-axis) was applied to the synthetic volume (Figure 4). The strain increment $\Delta\epsilon_{xx}$ ranged from 0.04 to 0.40% per voxel along the x-axis. This was chosen so that the maximum difference in strain due to non-uniformity within a box ranged from 4 to 40%. This range corresponds to the order of non-uniformity in literature, where differences in axial strain of more than 30% in a single fascicle have been reported (Englund et al., 2011, Shin et al., 2009, Blemker et al., 2005).

2.4. Statistics

The mean and standard deviation of the non-relative and relative error were calculated for both axial and shear strain. The accuracy was defined as the deviation of the mean error from zero. A positive mean error indicated that the strain tracker overestimates strain, a negative error indicated underestimation of strain. The precision was defined as the variance from the mean, and is represented by the standard deviation.

Statistical testing was done in SPSS (Version 25, IBM corp.). For the first simulation consisting of 100 runs per condition, the Shapiro and Wilk test was used to confirm normality of the error. One sample t-tests were performed to evaluate if the mean errors were biased, and significantly deviated from zero. For all the simulations, Fischer one-way

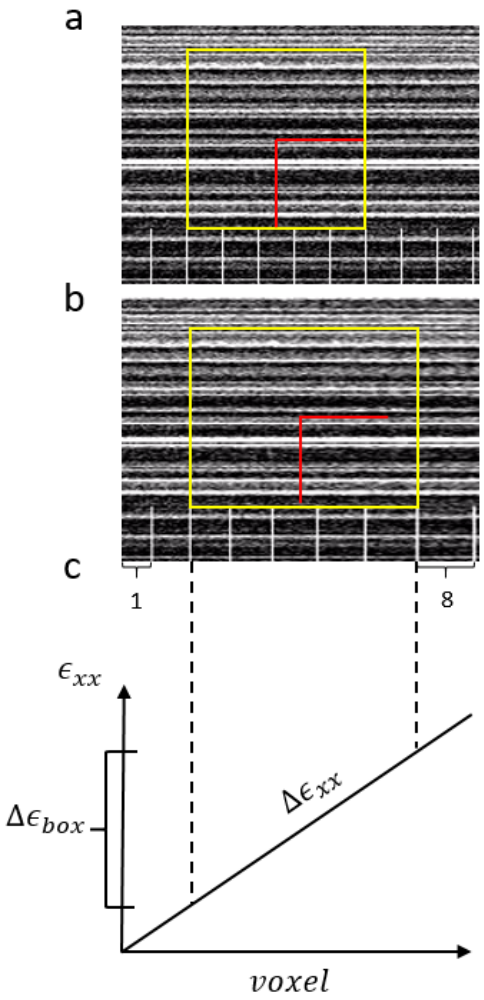

Figure 4. (a) A tracked virtual ultrasound image that is aligned with the fascicle direction before deformation. The yellow box has an initial size of 100 by 100 pixels. Vertical, white striations of equal spacing were added in the synthetic volume which can be observed in the bottom of the image. Tracked points are not shown. (b) A tracked ultrasound image after a non-uniform strain of $\Delta\epsilon_{xx} = 0.20\%$ per voxel was applied over the synthetic volume. Notice the difference in length of the first striation interval and the eighth, and how the spacing has progressively increased along the fascicle direction. (c). The course of the strain ϵ_{xx} along the fascicle direction in voxels is shown. The gradient is indicated by $\Delta\epsilon_{xx}$. The difference in strain between the utmost left and right side of the box is $\Delta\epsilon_{box}$ and equals $\Delta\epsilon_{xx} \cdot boxsize = 20\%$ for this case.

ANOVA was used to test whether the measured strains and amount of lost points were affected by the conditions. Post hoc analysis was performed using the Tukey honestly significant difference (HSD) test.

3. Results

3.1. Simulation 1: Combined axial and shear strain

Results of the error of the first simulation are shown in the boxplots of Figure 5. The boxplots are symmetrical and the error was normally distributed for each condition (Shapiro-Wilk, $p > 0.05$ for all conditions of strain).

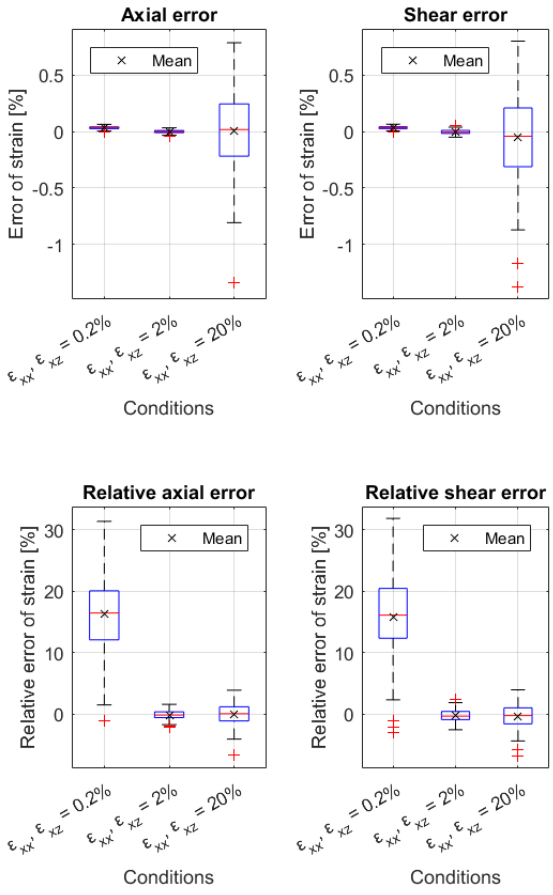

Figure 5. Boxplots for the error (top half) and relative error (bottom half) in the measurement of axial strain (left half) and shear strain (right half) are shown for three conditions of strain.

For all conditions of axial and shear strain, the absolute mean error was smaller than 0.06% strain. The absolute axial error was not significantly affected by the conditions, but the absolute shear error was significantly affected (One-way ANOVA, axial: $F(2, 297) = 0.866, p = 0.422$, shear: $F(2, 297) = 4.21, p = 0.016$). Post hoc testing indicated that only the absolute shear error for the 0.2% condition was significantly greater than the 20% condition ($p = 0.012$).

In absolute terms, the axial and shear strain were significantly overestimated for the 0.2% condition (t-test, axial: $t(99) = 29.6, p < 0.001$, shear: $t(99) = 24.0, p < 0.001$). For the 2% and the 20% condition, the measured axial strain was not biased (2% axial: $t(99) = -1.64, p = 0.104$, 20% axial: $t(99) = 0.74, p = 0.460$). The measured shear strain was underestimated for the 2% and 20% condition, but this was not significant (2% shear: $t(99) = -1.92, p = 0.580$, 20% shear: $t(99) = -1.51, p = 0.133$).

Both relative axial and relative shear error were significantly affected by the conditions (One-way ANOVA, axial: $F(2, 297) = 664.7, p < 0.001$, shear: $F(2, 297) = 559.5, p < 0.001$). The relative error of both axial and shear of the 0.2% strain condition were significantly greater than the 2% condition (axial $p < 0.001$, shear $p < 0.001$) and the 20% condition (axial: $p < 0.001$, shear: $p < 0.001$). The relative error of the 2% and 20% condition did not differ significantly for axial strain ($p = 0.968$) and shear strain ($p = 0.809$).

Absolute precision was lowest for the condition of largest imposed strain of 20%. The spread of the error for the condition of 20% strain (axial SD = 0.33%, shear SD = 0.37%) was greater than the spread of the error of the 2% strain condition (axial SD = 0.014%, shear SD = 0.020%) and the spread of the 0.2% condition (axial SD = 0.011%, shear SD = 0.013%). However, in relative terms, the spread of the error of the 20% condition (relative axial SD = 1.66%, relative shear SD = 1.86%), was more similar to the 2% condition (relative axial SD = 0.70%, relative shear SD = 1.01%). The spread of the relative error was highest for the 0.2% condition (relative axial SD = 5.54%, relative shear SD = 6.57%).

The average fraction of lost points was 0.00% for the 0.2% condition, 0.01% for the 2% condition, and 12% for the 20% condition. The conditions affected the amount of lost points (One-way ANOVA, $F(2, 297) = 280.9, p < 0.001$), but only differences between the 20% condition and the other two conditions of 2% and 0.2% were significant (20% and 2%: $p < 0.001$, 20% and 0.2%: $p < 0.001$).

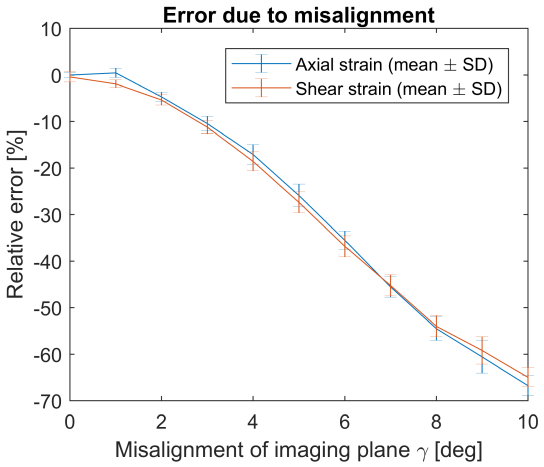

Figure 6. The relative error (mean ± SD) for different degrees of misalignment are shown. The mean relative error in axial strain (blue) and shear strain (red) decrease simultaneously from 0% to -65% over a misalignment angle γ ranging from 0°to 10°.

3.2. Simulation 2: Strain while the imaging plane is misaligned

Results for the relative error while the imaging plane is misaligned are shown in Figure 6.

The relative error became significantly more negative with increasing angles γ of plane misalignment (one-way ANOVA axial: $F(10, 319) = 4319.4$, $p < 0.001$, shear: $F(10, 319) = 4323.0$, $p < 0.001$). The total strain was a combined 2% axial and shear strain for all conditions of γ. A negative sign of the relative error indicates that the strain is underestimated. For a three degree misalignment, the relative error for axial and shear were -10.4 ± 1.63% and -11.7 ± 1.87% respectively. For a ten degree misalignment, the relative error of axial and shear strain were -66.8 ± 2.1% and -65.0 ± 2.1%.

The mean relative axial error was typically within one standard deviation of the mean relative shear error, and vice versa. A significant difference between the error in axial and shear strain was found for an angle γ of 1 degree ($p = 0.002$). For other angles of plane misalignment, there was no significant difference in the relative error.

For all conditions of plane misalignment from zero to ten degrees, the mean fraction of points lost was 0.00%.

3.3. Simulation 3: Rotational velocity of the imaging plane

Results for the relative error when the imaging plane was rotated are shown in Figure 7

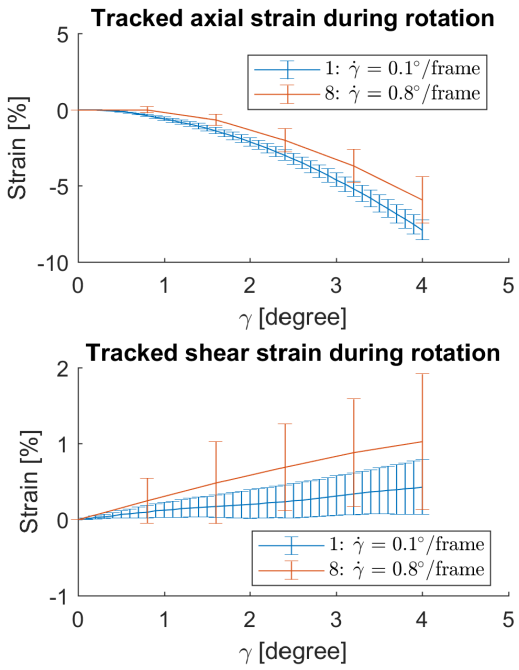

Figure 7. The error (mean ± SD) of axial strain (top) and shear strain (bottom) for different rotational velocities of the imaging plane.

Negative axial strain was measured as the image plane rotated away from the fascicle orientation. For the conditions of faster image plane rotation, lower values of axial strain were measured compared to slower rotations, for an equal total rotation. The measured axial strain was significantly affected by the rotational velocity for an angle γ of 4.0° (one-way ANOVA, $F(7, 232) = 13.33$, $p < 0.001$). For $\gamma = 4.0°$ rotation, the axial strain ranged from $-5.92 \pm 1.52\%$ (mean ± SD) for the fastest rotation ($\dot{\gamma} = 0.8°$/frame), to -7.90 ± 0.66% for the slowest rotation ($\dot{\gamma} = 0.1°$/frame).

Positive shear strain was measured as the imaging plane rotated. Contrary to axial strain, higher values of shear strain were measured for a faster rotation of the imaging plane, for an equal total rotation. The measured shear strain was significantly affected by rotational velocity for an angle γ of 4.0° (one-way ANOVA, $F(7, 232) = 3.31$, $p = 0.002$). The shear strain when the plane had rotated $\gamma = 4.0°$ ranged from 0.43 ± 0.36% strain for the slowest rotation ($\dot{\gamma} = 0.1°$/frame) to 1.03 ± 0.89% for the fastest rotation ($\dot{\gamma} = 0.8°$/frame).

Figure 8 shows the amount of points lost for the different rotational velocities. Most points were lost in the first consecutive frame (frame number 2).

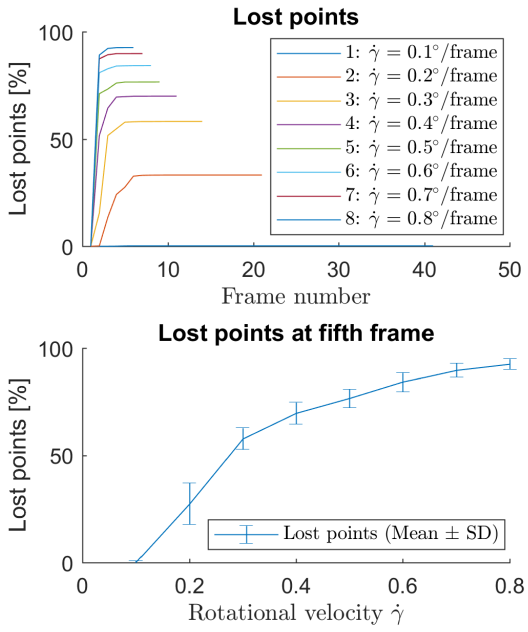

Figure 8. In the top figure, the mean fraction of lost points versus the frame number is shown for the range of rotational velocities. In the bottom figure, the fraction of lost points at the fifth frame for each velocity is shown.

The fraction of lost points was greater than 51% for the velocities ranging from 0.4 to 0.8° per frame. After the second frame, the amount of points lost decreased degressively and stabilized at the fifth frame.

For higher rotational velocity, the amount of points lost at the fifth frame increased significantly (one-way ANOVA, $F(7, 232) = 849.4$, $p < 0.001$). For the fastest rotation ($\dot{\gamma} = 0.8°$/frame), 92% of the points were lost at the fifth frame. For the slowest rotation ($\dot{\gamma} = 0.1°$/frame), 0% of the points were lost at the fifth frame.

3.4. Simulation 4: Non-uniform strain

Results of the simulation of linearly increasing axial strain are shown in Figure 9.

The relative error was significantly affected over the range of gradients $\Delta\epsilon_{xx}$ (One-way ANOVA, $F(9, 290) = 44.4, p < 0.001$). The relative axial error first increased and then decreased with the gradient $\Delta\epsilon_{xx}$. For gradients $\Delta\epsilon_{xx}$ between 0.04% and 0.16% strain per voxel, the relative error was positive. The mean relative error was maximally 15.5%. When the gradient $\Delta\epsilon_{xx}$ increased to values over 0.16% strain per voxel, the relative error decreased. The mean relative error decreased to a minimum of -59.4% for the steepest gradient $\Delta\epsilon_{xx}$ of 0.40% strain per voxel.

The standard deviation of the relative error was greater for higher values of the gradient $\Delta\epsilon_{xx}$. For $\Delta\epsilon_{xx} = 0.16\%$/voxel, the standard deviation was 1.48%. For $\Delta\epsilon_{xx} = 0.40\%$/voxel, the standard deviation was 17.7%. The amount of lost points increased significantly for higher gradients of strain (one-way ANOVA, $F(9, 290) = 856.6, p < 0.001$). Up to a gradient of $\Delta\epsilon_{xx}$ of 0.08% per voxel, the mean percentage of lost points was 0.00%. At a gradient $\Delta\epsilon_{xx}$ of 0.12% per voxel, the mean percentage of lost points was 4.3%. The mean percentage of lost points continued to increase to a value of 73% for a gradient of 0.40% strain per voxel.

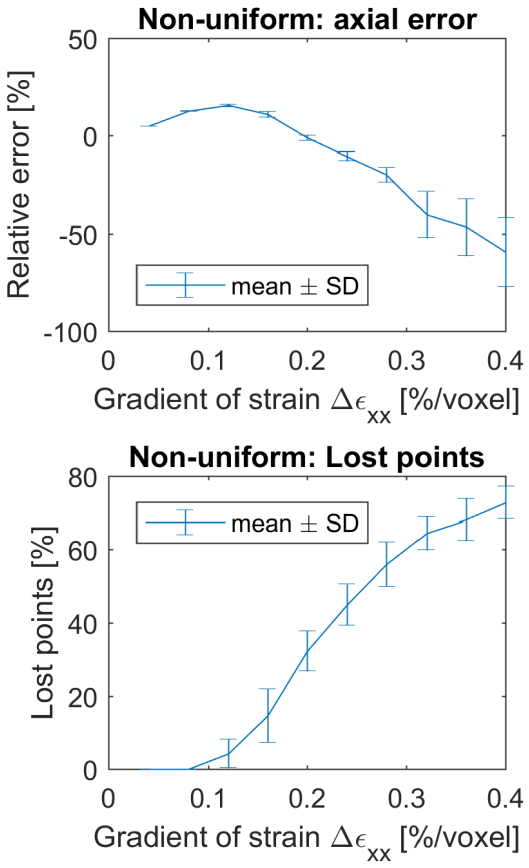

Figure 9. The top figure shows the relative error of axial strain for increasing gradients of non-uniform strain. The bottom figure shows the amount of points that were lost for the conditions.

4. Discussion

The goal of the present study was to validate strain tracking in the muscle from ultrasound images. Potential sources of error were investigated. When the imaging plane remained motionless and was aligned with the fascicle (simulation 1), the absolute mean error for both shear and axial strain were less than 0.06% strain for all the conditions of imposed strain of 0.2%, 2% and 20%. Relative error and relative standard deviation of both axial and shear strain were smaller than 0.3% and 1.9% for the conditions of 2% and 20% strain, respectively. For a misalignment of angle γ ranging from zero to ten degrees and a combined 2% strain (simulation 2), the axial and shear strain were underestimated by up to 65%. When the imaging plane rotated (simulation 3), the fraction of points lost in the first consecutive frame was greater than 51% for velocities $\dot{\gamma}$ ranging from 0.4 to 0.8°/frame. For non-uniform strains (simulation 4) where the difference in strain was between 4% and 16% over the ROI, the axial strain was overestimated by maximally 15.5% per frame.

4.1. Simulation 1: Combined axial and shear strain

Axial and shear strain can be distinguished by the strain tracker. Applying various combinations of combined axial and shear strain did not lead to systematic measurement errors in absolute or relative terms. This follows from the result that the absolute mean error in axial and shear measurement was smaller than 0.06% strain for the three conditions of imposed strain of 0.2%, 2% and 20%.

The strain tracker performs best for strain in the order of 2% and 20%. Errors in strain measurement were related to the imposed strain. The errors were less for the smaller strain of 2%. However, a limit to the accuracy and precision of the tracker was found. The condition of 0.2% strain showed a higher value of absolute mean error and a similar spread of the error as the 2% condition, indicating that a minimum of both the absolute error and spread of the error was obtained for the 2% condition. In relative terms, the 0.2% strain condition resulted in highest errors (16% for both axial and shear) and highest spread of the error. As a result, the strain tracker is best used when the strain is greater than 0.2% and the desired deviation of the error is greater than 0.02%. For the 100 pixel sized ROI used in this study, the minimum strain corresponds to a strain of 0.2 pixels and a deviation greater than 0.02 pixels.

The order of the error is comparable to other studies that have used DIC to quantify strain in biological tissue from optical images (Amiot et al., 2013, Boyle et al., 2014, Palanca et al., 2015). In these studies, DIC was optimized for optical images and not for ultrasound images. Okotie et al. (2012) compared three methods for the quantification of strain in rat tendon; manual calculation using markers, DIC from optical images and DIC from ultrasound images. No significant differences in strain measurements between the methods were found, suggesting that DIC from optical and ultrasound images have comparable accuracy. In a comparison of nine different optical DIC packages, the systematic displacement in low noise conditions was found to be roughly 0.01 pixel (Amiot et al., 2013). The 0.01 pixel systematic error corresponds to the order of the absolute error expressed in pixels found in this study (axial; 0.033, 0.0023, 0.0091 pixel, shear; 0.031, 0.0040, 0.056 pixel, for the 0.2%, 2% and 20% conditions respectively). Boyle et al. (2014) investigated the error in strain using the KLT algorithm in a condition of axial strain combined with a rigid body rotation. The reported error in strain was in the order of 0.01% between two consecutive frames, for which the imposed axial strain was 0.25%. The reported error for 0.25% strain (error 0.01%) lies in between the error of the 0.2% (error 0.032%) and 2% (error 0.0022%) strain conditions of the current study. Additionally, a precision of 0.11% and systematic error of 0.01% were reported in a study where DIC was calibrated for the study of human vertebrae (Palanca et al., 2015). The reported precision of 0.11% is in between the precision of the 2% (0.014%) and the 20% (0.33%) conditions of the current study. In summary, when the imaging plane is aligned with the fascicles ($\gamma = 0°$), strain tracking from ultrasound has a sub-pixel accuracy and precision, similar to that of existing DIC applications.

4.2. Simulation 2: Strain while the imaging plane is misaligned

Large errors were introduced when the imaging plane was not aligned with the fascicle. Axial and shear strain were underestimated by at least 10% and 65% for a three and ten degree misalignment respectively.

Part of the underestimation of strain due to misalignment can be explained by the projection of 3D

strain onto the 2D imaging plane. For an axial strain of the fascicle in 3D, the ratio of 3D strain to the 2D strain in the imaging plane is described by the cosine of the misalignment angle. For a ten degree misalignment, the strain measured in the 2D imaging plane is a fraction of $cos(10^\circ) = 0.985$ of the fascicle strain in 3D. This corresponds to an relative error of -1.5%, which is far from the underestimation of -65% found in the simulations.

Other studies have investigated the effect of transducer orientation on fascicle length, but not for fascicle strain in a dynamic condition of the muscle (Klimstra et al., 2007, Kellis et al., 2009, Bénard et al., 2009, Bolsterlee et al., 2016). In fascicle tracking, fascicle length can be overestimated when different fascicle sections in the image are regarded as a one continuous fascicle. In strain tracking, only a fraction of the strain can be measured, which is maximally 100% when the strain occurs exactly in the imaging plane. Results of the simulation confirm that imaging plane misalignment caused only underestimation of strain, and not overestimation. It can be concluded that errors in strain tracking are not comparable to errors in fascicle length measurement.

The high error due to misalignment can be explained by parts of the muscle that move in and out of the ultrasound image. Upon axial strain of the fascicles, the imaging plane does not align with the deforming material plane that was initially imaged (Figure 10). Parts of the muscle move in, and other parts move out of the imaging plane. In the resulting image, sections of the fascicles remain of similar geometry, while speckles flow in and out. Tracked speckles that move out of the imaging plane are not lost (0.00% points were lost for all degrees of misalignment). This is because the sections have a similar geometric appearance, causing points to be falsely recognized. As the angle γ of misalignment increases, speckles move in and out over a shorter distance in the imaging plane. The result is that more points are falsely recognized, and less strain is tracked.

A substantial error in strain due to misalignment of the imaging plane with the fascicle is expected for real ultrasound measurements. In half of the measurements on cadavers, Bénard et al. (2009) reported a misalignment of 15 degrees of the imaging plane with the plane of the fascicles. However, the angle of the fascicles within the fascicle plane is not given, and therefore the misalignment of the imaging plane with the fascicles is not known. Bolsterlee et al. (2015) compared architectural measurements from ultrasound with diffusion tensor images and found that fascicles were oriented on average 5.5 $\pm$ 4.4° to the ultrasound imaging plane. Misalignment of the fascicles with the imaging plane ranged from 0° to 10.8° for 90% of the measurements. For this range of misalignment, strains measured by the tracker would be underestimated from 0% to more than 65%, and on average 30%. The large effect of misalignment emphasizes the need for careful positioning of the ultrasound transducer with the fascicle orientation. Consequently, anatomical information about the muscle structure is required to determine the transducer orientation that minimizes error.

4.3. Simulation 3: Rotational velocity of the imaging plane without deformation

Rotation of the imaging plane led to measurement of strain. An axial strain ranging from -5.9% to -7.9% was measured for angular velocities from 0.1 degree/frame to 0.8 degree/frame over a total displaced angle of 4 degrees. The shear strain averaged less than 1.0% for all angular velocities.

In real ultrasound measurements, relative rotation of the transducer to the muscle unlikely leads to substantial measurement of strain. More than 50% of points could not be tracked within the first two frames for velocities higher than 0.3 degree/frame. This means that for higher rotational velocities, the point tracker performed well since it did not recognize features from a different muscle structure. Losing more than 50% of the points within a consecutive frame should be interpreted as a warning that a different structure is imaged. For rotational velocities of 0.3 degree/frame and slower, an acceptable fraction ($< 50\%$) of points were lost for the first two frames. Only for the slowest rotational velocity of 0.1 degree/frame, the fraction of points lost remained below 30% over the total 4 degree rotation. For lower rotational velocities, it requires more frames to accumulate the same error. A substantial error, without losing a high fraction of points, can therefore only be caused when the plane is rotated with a constant velocity in a small range ($< 0.3^\circ$/frame), and for a prolonged period (e.g. more than 20 frames for a velocity of 0.1°/frame to obtain error of 2% axial strain). It is unlikely that in real ultrasound measurements, relative rotation of the imaging plane with the muscle occurs constantly, for a prolonged period, and exactly in a particular range.

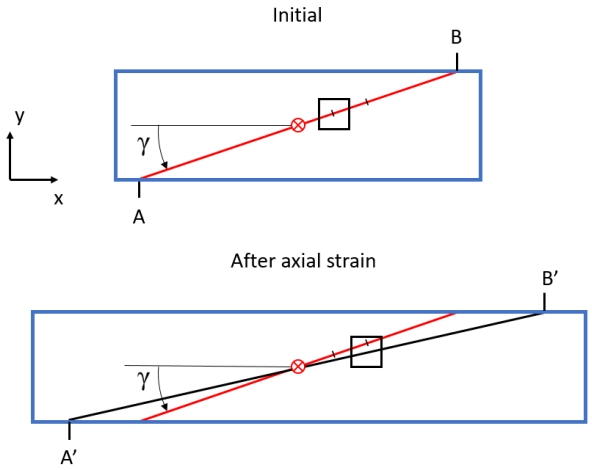

Figure 10. A simplified top view of the synthetic volume (blue) and imaging plane (red). The top shows the configuration before the volume is deformed, the bottom after the volume has been strained axially in x-direction. The imaging plane is misaligned with the fascicle direction (x) with the same angle γ for both configurations. The red cross marks the center of the imaging plane and the black square represents a voxel in the volume. Voxels are interpolated over the imaging grid to form an image. Black dashes on the red line of the imaging plane denote two locations of the interpolation grid. The letters A and B mark positions on the material, the line AB represents a material line. The positions A and B flow with the material, and are denoted A' and B' after deformation. After deformation, the line A'B' is not coincident with the imaging plane anymore, and the voxel has moved to the right. The center of the voxel does not coincide with the center of the second interpolation dash. Consequently, neighboring voxels will influence the brightness value that corresponds to that pixel in the image. The results is that a slightly different section of the material is imaged. If the material is to strain further, the voxel would move further to the right. The voxel could move far enough so that it does not influence the 2D image anymore. In this manner, tracked voxels can move out of the imaging plane when a strain is applied. For higher angles γ, the distance over which voxels run out of the imaging plane decreases, and the strain becomes more difficult to track.

In real ultrasound measurements, the trajectories and velocities of the imaging plane likely differ from the simulation. In the simulation, limits of the strain tracker were tested in a worst case scenario. The trajectory of the imaging plane was chosen so that fascicles appeared to shorten, while in fact their length remained unchanged (Appendix C). The image plane rotated around one axis with a constant rotational velocity. In reality, disturbing movements of the transducer will more likely result into a combination of rotations with variable velocities around more than one axis. It is expected that for such disturbing movements the fraction of lost points increases even more. Therefore, movement artifacts unlikely result into substantial error without the user being aware that the measurement is invalid.

4.4. Simulation 4: Non-uniform strain

Errors in strain measurement are introduced when non-uniform strain fields are measured. For small gradients of linearly increasing strain ($\Delta\epsilon_{xx} <$ 0.16%), the tracker overestimates the strain by up to 15%. For gradients higher than 0.16%, the strain was underestimated up to a value of 60% for a gradient of 0.40%/voxel. When the degree of non-uniform axial strain is high, the strain tracker will not be able to accurately measure axial strain. For gradients higher than 0.08%/voxel, the fraction of points lost increased substantially. Points were lost because they did not fit the estimated transform, but not because features could not be recognized. It is not surprising that for a non-uniform strain field points were lost, since the transformation estimated by the MSAC algorithm is linear. The maximum pixel distance setting of the MSAC algorithm will influence the amount of lost points when a non-uniform strain field is measured. It is recommended that this setting is set to low values (=< 2 pixels). Losing points is then not only a warning that a different structure is imaged, but also that the strain field is possibly non-uniform.

The high non-uniform strain patterns reported in the literature Englund et al. (2011), Shin et al. (2009), Blemker et al. (2005), could lead to an error in strain measurement. A model of the biceps brachii showed that, for active contraction, fiber stretch was 1.6 in the proximal area, while in the distal area the fiber stretch was 1.0 (Blemker et al., 2005). In eccentric contraction of the gastrocnemius, an approximate difference of 100% strain between the distal and proximal area has been reported (Shin et al., 2009). The reported differences in strain are substantially higher than the 8% difference in strain (corresponding to a gradient of 0.08% and a box size of 100 pixels), at which points are lost. However, the reported differences in strain are over the whole length of the muscle, while the box tracks the strain for a smaller section. In addition, the degree of non-uniformity between frames will not only depend on the difference in strain but also on the frame rate of the ultrasound measurement. This is because for a given strain, a higher number of frames will lead to smaller differences in strain between consecutive frames. The degree of non-uniformity between frames is assumed to be

less than the 0.08%/voxel gradient (e.g., in a US video consisting of 100 frames and a strain difference of 100% over the box, the corresponding gradient equals 100% strain / 100 frames / 100 pixel size box = 0.01% strain per pixel). For the non-uniformity expected in in the muscle (gradient < 0.08%/voxel), the strain tracker will not lose points but errors may accumulate over the frames. In real ultrasound measurements of the muscle, non-uniform axial strain will likely lead to overestimation of strain.

4.5. Linking the simulations

To minimize tracking errors a lower frame rate is preferred. In three of the four simulations, the error was explored for two consecutive frames. For ultrasound measurements consisting of multiple frames, each frame introduces the possibility of an error. Consequently, the error in strain will accumulate over the frames (Boyle et al., 2014). The frame rate of ultrasound videos typically ranges from 10 to 100 frames per second. Between frames, the strain and non-uniformities are expected to be small. Ideally, the frame rate is the minimum while points are not lost and conditions for lowest error are met. The lowest error is obtained when strain in the muscle is uniform and in the order of 2% between frames, while the imaging plane remains steady and is aligned with the fascicle. The algorithm could be potentially be improved so that it first roughly estimates the strain, but only calculates the strain for selected frames in which the strains approximate 2%.

The highest errors are reported for the condition when the imaging plane is misaligned with the fascicles. This type of error is likely to occur in real ultrasound measurement, and to contribute most to the total error. Relative errors up to 65% are to be expected. However, model parameters may particularly affect the results for this simulation. If errors strongly depend on the geometry of the synthetic volume or speckle pattern, it will be questionable to what extent results from the simulation translate to real ultrasound measurements. Parameters of the model should then be chosen more accurately.

4.6. Model limitations

Model parameters will most likely affect the results for the simulations where the imaging plane misaligns with the fascicles (simulation 2) or rotates relative to the muscle (simulation 3). In these simulations the imaging plane makes use of the three dimensions of the synthetic volume.

Fascicle structure and speckle pattern intensity play an important role in tracking of points. Additional simulations have revealed that points were not lost when the imaging plane was oriented perpendicular to the fascicle direction ($\gamma = 90°$), and then translated along the fascicle direction (x). However, when the synthetic volume contained no fascicles but only a speckle pattern, points were rapidly lost in the same simulation. This confirms that points are falsely recognized for images with similar sections of the fascicles, as observed in the misalignment simulation (simulation 2). A trade-off between fascicle geometry and speckle pattern exists, that determines if points are falsely recognized or not. The model parameters that determine fascicle structure and intensity of the speckle pattern affect the error in strain measurement. Larger fascicle radii lead to longer cross section of fascicles, but also to smoother brightness gradients (Appendix D). Both are expected to affect traceability when the plane is misaligned. A greater intensity of the speckle pattern, could lead to better traceable points and prevent recognition of false points.

4.7. Future work

For future simulations it is advised that modelling parameters, in particular for the speckle pattern, are chosen more accurately. Model parameters were initially chosen arbitrarily. The speckle pattern parameter σ_{gran} influences traceability of points. A better estimation of the speckle pattern parameter σ_{gran} can be obtained by analyzing the speckle distribution of real ultrasound images. Additionally, a more realistic model for speckle generation could be applied. A suggestion is to model the speckles as family wise noise; groups of pixels with correlated brightness values. A speckle radius of 3-5 pixels has been shown to result in low systematic error (Sutton et al., 2009, Amiot et al., 2013). When the features to be tracked are bigger, they have a higher chance to intersect the imaging plane and influence brightness of the image. This is expected to particularly influence results when the plane is misaligned with the fascicle.

Parameters for the structure of the synthetic volume should be determined more accurately as well. The fascicle diameter was with 3 pixels on the smaller side. By counting the thickness of the fascicles from an ultrasound video of the gastrocnemius

muscle (Appendix A), the diameter was found to be 6-12 pixels. These parameters will, however, differ based on the subject and the ultrasound equipment used. Another suggestion is to add variability in the pennation angle or curvature of the fascicles that results in a more realistic muscle structure. This will break the symmetry in the fascicle direction, making false recognition in the fascicle direction less probable. Instead of improving the model, real three dimensional ultrasound data for the simulations could be used. Moreover, real time 3D ultrasound allows the tracking of strain based on digital volume correlation (DVC), for which misalignment errors would be avoided completely.

5. Conclusion

A strain tracking algorithm for the quantification of strain from two-dimensional ultrasound images was developed for this study. The strain tracker provides accurate and precise measurements of axial and shear strain when the imaging plane is aligned with the fascicle plane. Rotation of the ultrasound transducer relative to the muscle during acquisition results in invalid measurements. Non-uniform strain patterns in the muscle may lead to overestimation of axial strain. Largest errors are introduced when the imaging plane is misaligned with the fascicle. Consequently, anatomical information about the muscle structure is required to align the imaging plane with the fascicles and minimize errors in strain tracking.

6. Acknowledgements

Thank you Huub and Winfred, for your supervision throughout the project. Your down to earth feedback has led to numerous improvements, I have learned a lot from it. Thank you Cor, for your brainstorming sessions with continuum mechanics. Thank you team Sydney, Bart and Rob, for making me feel welcome. It was your enthusiasm that inspired me to pursue this project. Bart, thank you for your mentorship.

7. References

Amiot, F., Bornert, M., Doumalin, P., Dupr, J., Fazzini, M., Orteu, J., Poilne, C., Robert, L., Rotinat, R., Toussaint, E., 2013. Assessment of digital image correlation measurement accuracy in the ultimate error regime: main results of a collaborative benchmark. Strain 49 (6), 483–496.

Azizi, E., Brainerd, E. L., Roberts, T. J., 2008. Variable gearing in pennate muscles. Proceedings of the National Academy of Sciences 105 (5), 1745–1750.

Barber, L., Hastingsison, T., Baker, R., Barrett, R., Lichtwark, G., 2011. Medial gastrocnemius muscle volume and fascicle length in children aged 2 to 5 years with cerebral palsy. Developmental medicine & child neurology 53 (6), 543–548.

Bénard, M. R., Becher, J. G., Harlaar, J., Huijing, P. A., Jaspers, R. T., 2009. Anatomical information is needed in ultrasound imaging of muscle to avoid potentially substantial errors in measurement of muscle geometry. Muscle & Nerve: Official Journal of the American Association of Electrodiagnostic Medicine 39 (5), 652–665.

Blemker, S. S., Pinsky, P. M., Delp, S. L., 2005. A 3d model of muscle reveals the causes of nonuniform strains in the biceps brachii. Journal of Biomechanics 38 (4), 657–665.

Bolsterlee, B., D'Souza, A., Gandevia, S. C., Herbert, R. D., 2017. How does passive lengthening change the architecture of the human medial gastrocnemius muscle? Journal of Applied Physiology 122 (4), 727–738.

Bolsterlee, B., Gandevia, S. C., Herbert, R. D., 2016. Effect of transducer orientation on errors in ultrasound image-based measurements of human medial gastrocnemius muscle fascicle length and pennation. PLOS ONE 11 (6), e0157273.

Bolsterlee, B., Veeger, H. E. J., Van Der Helm, F. C. T., Gandevia, S. C., Herbert, R. D., 2015. Comparison of measurements of medial gastrocnemius architectural parameters from ultrasound and diffusion tensor images. Journal of Biomechanics 48 (6), 1133–1140.

Boyle, J. J., Kume, M., Wyczalkowski, M. A., Taber, L. A., Pless, R. B., Xia, Y., Genin, G. M., Thomopoulos, S., 2014. Simple and accurate methods for quantifying deformation, disruption, and development in biological tissues. Journal of The Royal Society Interface 11 (100), 20140685.

Criscione, C. J., Douglas, S. A., Hunter C., W., 2001. Physically based strain invariant set for materials exhibiting transversely isotropic behavior. Journal of the Mechanics and Physics of Solids 49 (4), 871–897.

Eby, S. F., Cloud, B. A., Brandenburg, J. E., Giambini, H., Song, P., Chen, S., LeBrasseur, N. K., An, K.-N., 2015. Shear wave elastography of passive skeletal muscle stiffness: Influences of sex and age throughout adulthood. Clinical Biomechanics 30 (1), 22–27.

Englund, E. K., Elder, C. P., Xu, Q., Ding, Z., Damon, B. M., 2011. Combined diffusion and strain tensor mri reveals a heterogeneous, planar pattern of strain development during isometric muscle contraction. American Journal of Physiology-Regulatory, Integrative and Comparative Physiology 300 (5), R1079–R1090.

Farris, D. J., Lichtwark, G.A., 2016. Ultratrack: Software for semi-automated tracking of muscle fascicles in sequences of b-mode ultrasound images. Computer methods and programs in biomedicine 128, 111–118.

Herbert, R. D., Bolsterlee, B., Gandevia, S. C., 2018. Passive changes in muscle length. Journal of Applied Physiology 0 (0), null.

Hoang, P., Saboisky, J., Gandevia, S., Herbert, R., 2009. Passive mechanical properties of gastrocnemius in people with multiple sclerosis. Clinical Biomechanics 24 (3), 291–298.

Huijing, P. A., 1999. Muscle as a collagen fiber reinforced composite: a review of force transmission in muscle and whole limb. Journal of biomechanics 32 (4), 329–345.

Jakubowski, K. L., Terman, A., Santana, R. V. C., Lee, S. S. M., 2017. Passive material properties of stroke-impaired plantarflexor and dorsiflexor muscles. Clinical Biomechanics 49, 48–55.

Kellis, E., Galanis, N., Natsis, K., Kapetanos, G., 2009. Validity of architectural properties of the hamstring muscles: Correlation of ultrasound findings with cadaveric dissection. Journal of Biomechanics 42 (15), 2549–2554.

Klimstra, M., Dowling, J., Durkin, J. L., MacDonald, M., 2007. The effect of ultrasound probe orientation on muscle architecture measurement. Journal of Electromyography and Kinesiology 17 (4), 504–514.

Kwah, L. K., Herbert, R. D., Harvey, L. A., Diong, J., Clarke, J. L., Martin, J. H., Clarke, E. C., Hoang, P. D., Bilston, L. E., Gandevia, S. C., 2012. Passive mechanical properties of gastrocnemius muscles of people with ankle contracture after stroke. Archives of Physical Medicine and Rehabilitation 93 (7), 1185–1190.

Lee, S. S. M., Gaebler-Spira, D., Zhang, L. Q., Rymer, W. Z., Steele, K. M., 2016. Use of shear wave ultrasound elastography to quantify muscle properties in cerebral palsy. Clinical Biomechanics 31, 20–28.

Okotie, G., Duenwald-Kuehl, S., Kobayashi, H., Wu, M.-J., Vanderby, R., 2012. Tendon strain measurements with dynamic ultrasound images: Evaluation of digital image correlation. Journal of Biomechanical Engineering 134 (2), 024504–024504–4.

Palanca, M., Brugo, T. M., Cristofolini, L., 2015. Use of digital image correlation to investigate the biomechanics of the vertebra. Journal of Mechanics in Medicine and Biology 15 (02), 1540004.

Pan, B., Qian, K., Xie, H., Asundi, A., 2009. Two-dimensional digital image correlation for in-plane displacement and strain measurement: a review. Measurement science and technology 20 (6), 062001.

Purslow, P. P., Trotter, J. A., 1994. The morphology and mechanical properties of endomysium in series-fibred muscles: variations with muscle length. Journal of Muscle Research & Cell Motility 15 (3), 299–308.

Sharafi, B., Blemker, S., 2011. A mathematical model of force transmission from intrafascicularly terminating muscle fibers. Journal of biomechanics 44 (11), 2031–2039.

Shi, J., Tomasi, 1994. Good features to track. In: 1994 Proceedings of IEEE Conference on Computer Vision and Pattern Recognition. pp. 593–600.

Shin, D. D., Hodgson, J. A., Edgerton, V. R., Sinha, S., 2009. In vivo intramuscular fascicle-aponeuroses dynamics of the human medial gastrocnemius during plantarflexion and dorsiflexion of the foot. Journal of Applied Physiology 107 (4), 1276–1284.

Street, S. F., 1983. Lateral transmission of tension in frog myofibers: a myofibrillar network and transverse cytoskeletal connections are possible transmitters. Journal of cellular physiology 114 (3), 346–364.

Sutton, M., Orteu, J., Schreier, H., 2009. Dic. image correlation for shape, motion and deformation measurements: Basic concepts, theory and applications. New YorN: Springer 83.

Tomasi, C., Kanade, T., 1991. Detection and tracking of point features. Tech. Rep. CMU-CS-91-132, Carnegie Mellon University.

Torr, P. H., Zisserman, A., 2000. Mlesac: A new robust estimator with application to estimating image geometry. Computer vision and image understanding 78 (1), 138–156.

Appendix A. Application of the strain tracker

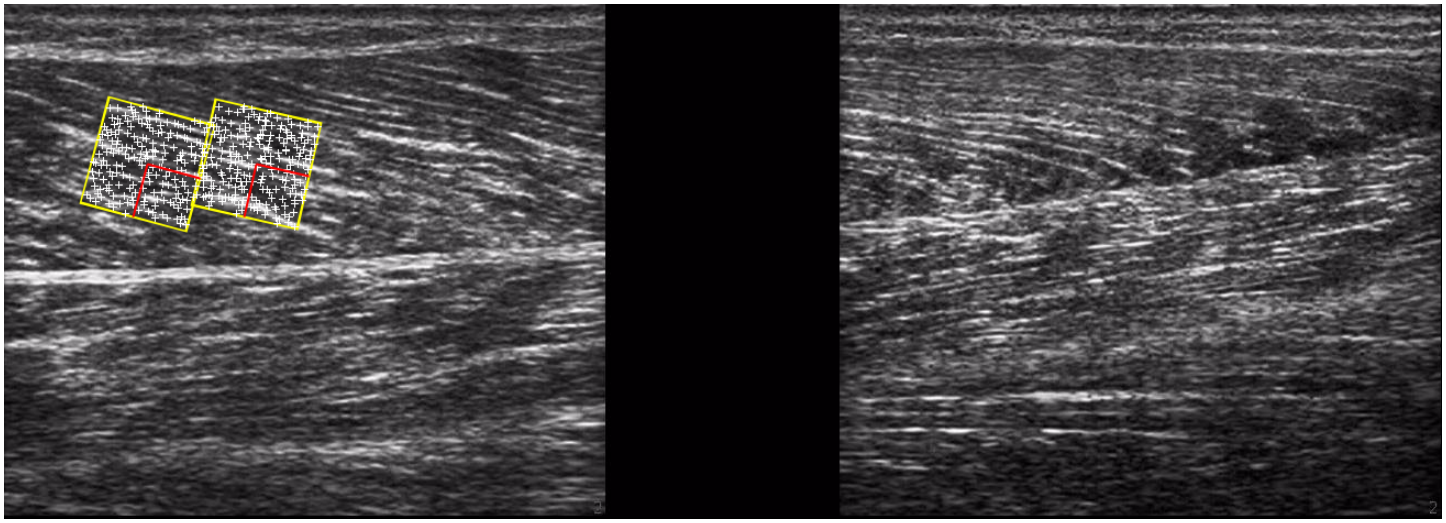

Figure A.11. The strain tracker is applied to an ultrasound video. The first frame prior to passive lengthening of the medial gastrocnemius is shown. The two yellow boxes enclose the tracked area in which points are tracked (white markers). The boxes are placed in the muscle tissue, in between the internal tendons. The internal tendons are visible as the two thick, bright lines running horizontally across the image. The smaller white striations within the muscle represent the fascicles. The perpendicular red lines of the boxes indicate the local axes system that is aligned with the fascicle direction.

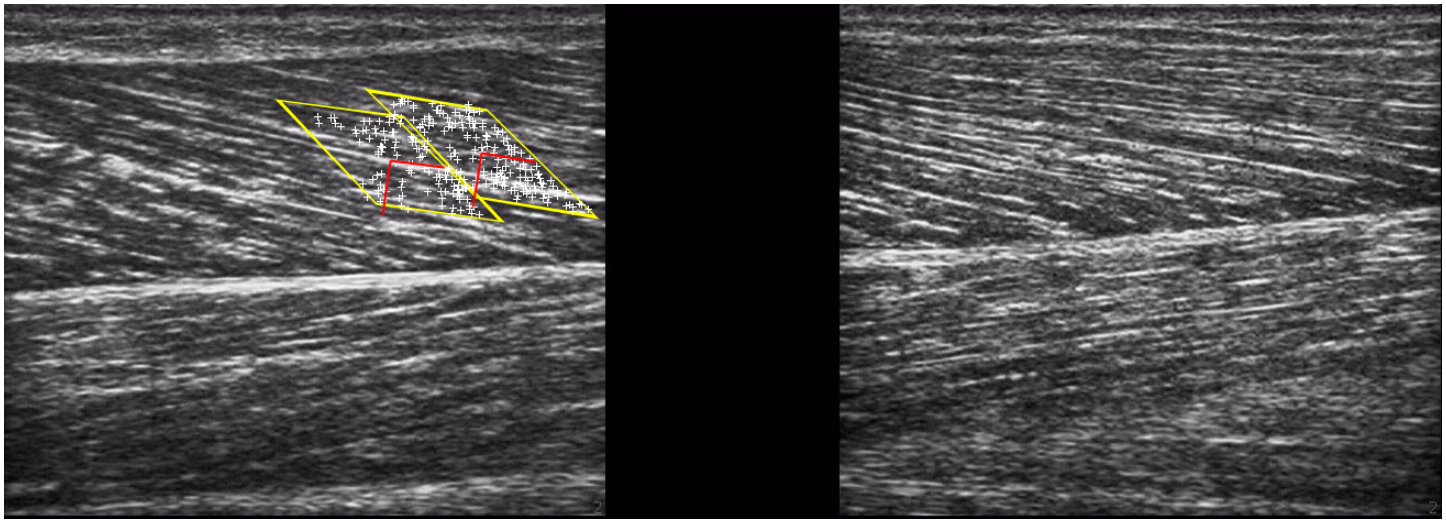

Figure A.12. An ultrasound frame (frame n = 150) after passive lengthening of the gastrocnemius muscle. The tracked areas (yellow squares) have translated to the right and exhibit a sheared configuration. Some points in the boxes have been lost throughout tracking of video frames.

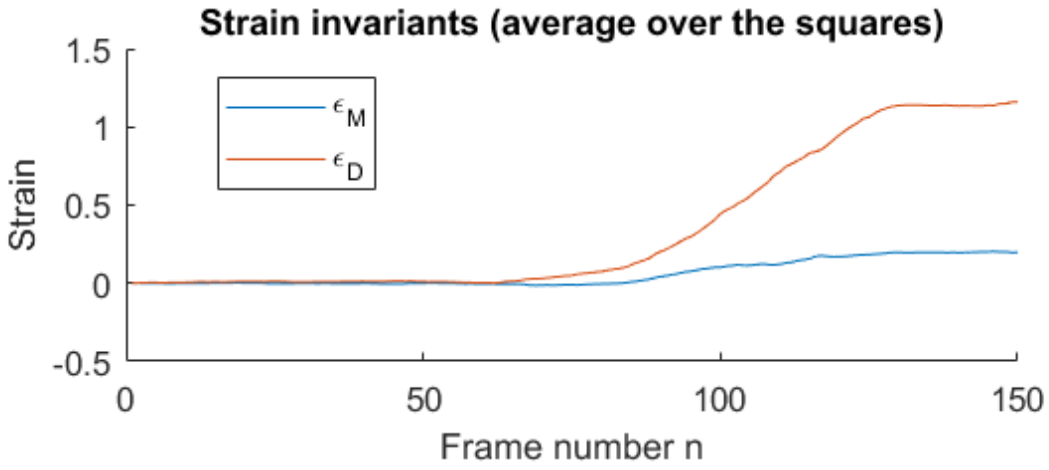

Figure A.13. The calculated strain plot against frame number. The fibre strain ϵ_M is shown in blue and the along fibre shear strain ϵ_D in red. From frame 60 onwards, the muscle is passively lengthened. The calculated fibre strain remains relatively small while the along fiber shear rises. The final values are approximately 0.1 and 1.2 for the fibre strain and along fibre shear strain respectively. Due to plane misalignment the strain may be underestimated; the actual strain that occurs in the muscle could be even higher.

Appendix B. Examples of simulation 1

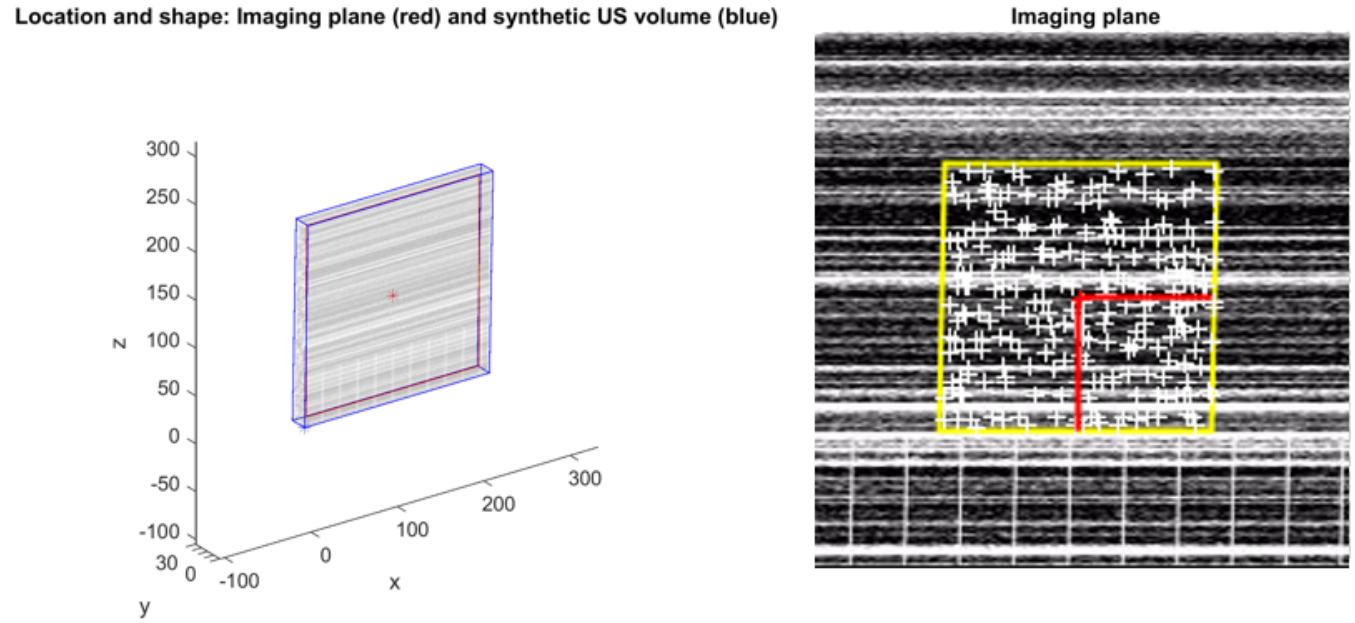

Figure B.14. On the left, an example of the configuration of the imaging plane and synthetic volume is shown as used for simulation 1. The configuration is after the synthetic volume has been strained by 2% shear and axial ($\epsilon_{xx}, \epsilon_{xz} = 2\%$). The synthetic volume was made only 20 voxels thick in y-direction to reduce the required computing power for the 100 runs that were performed. The right shows a corresponding frame which has been tracked. The applied axial and shear strain of 2% is barely visible. Strains were accurately tracked with mean relative errors in the order of 0.1% and absolute errors in the order of 0.01 pixel

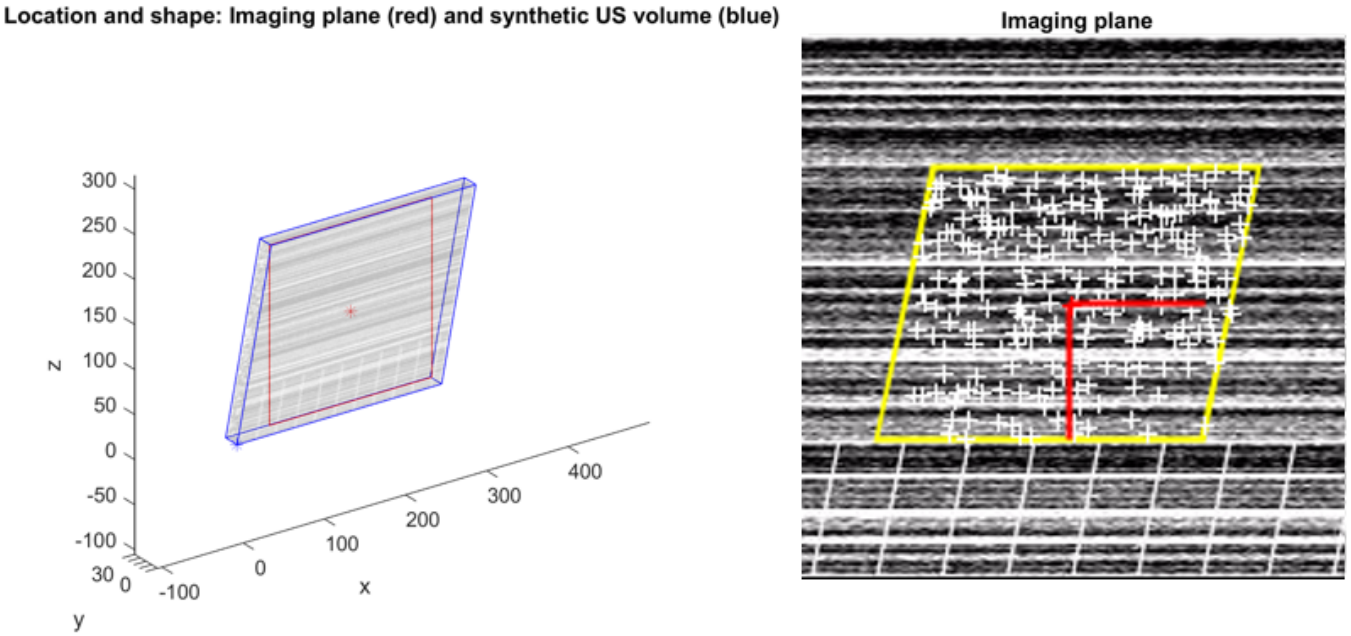

Figure B.15. The left shows the configuration after 20% strain has been applied ($\epsilon_{xx}, \epsilon_{xz} = 20\%$). On the right, a corresponding tracked frame is shown. The shear strain is now visible, indicated by the vertical striations that are under an angle. Some points were lost in the lower left and right corner of the yellow box. On average, 12% of the points were lost between a first frame (n = 1) and a follow up frame (n = 2, shown here) for strains of 20%. The absolute accuracy and precision decreased for higher strains; the 20% strain condition showed higher mean error and spread of the error than the 2% condition. However, the relative error of the 20% strain conditions was comparable to that of the 2% condition.

Appendix C. Misalingment of imaging plane with the fascicles

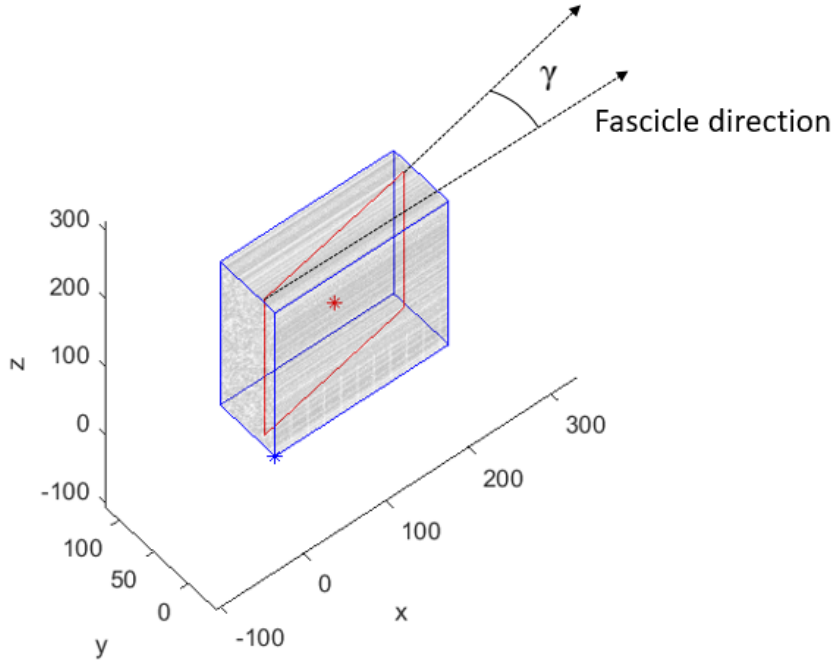

Figure C.16. The synthetic volume is in the initial, undeformed configuration, the imaging plane makes an angle γ of 10° with the fascicles. In simulation 2, an axial and shear strain of 2% was applied for angles γ ranging from zero to ten degrees.

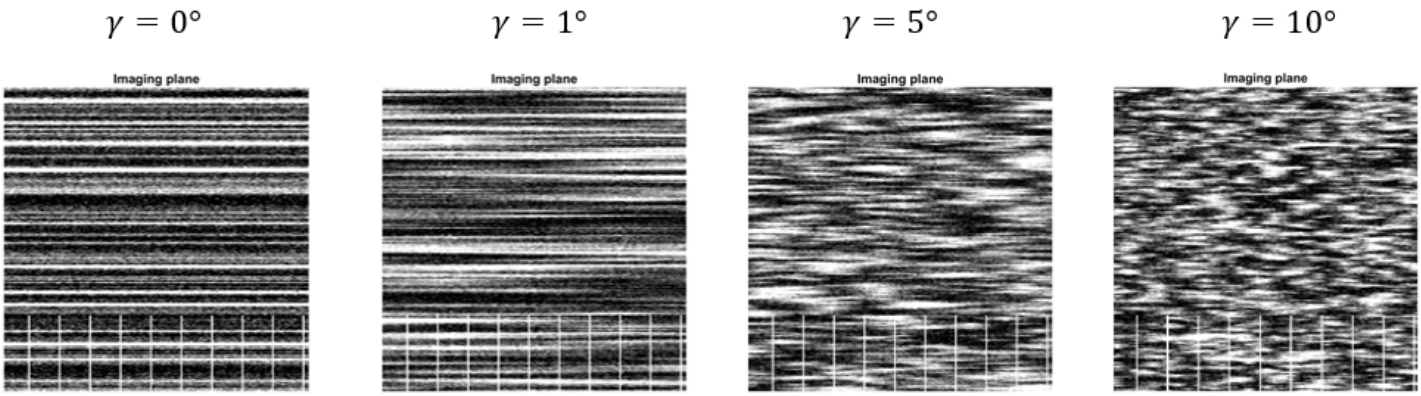

Figure C.17. Four ultrasound images for angles γ of 0°, 1°,5° and 10° are shown. As the angle γ of misalignment increases, the visible sections of the fascicles become shorter (simulation 3). For a ten degree misalignment, the length of the fascicle section is only a fraction of the true fascicle length. Synthetic volume modelling parameters, such as the radius of the fascicles, will affect the length of the section that is visible when the imaging plane is misaligned.

Appendix D. Synthetic volumes generated with larger fascicles

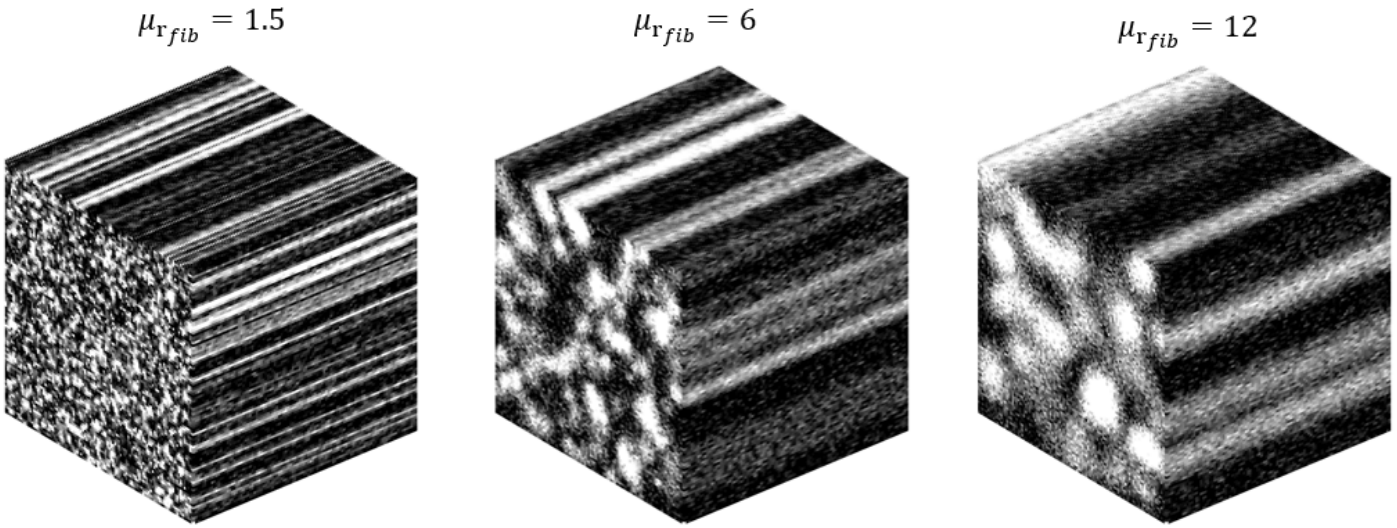

Figure D.18. Three synthetic volumes of 100x100x100 voxels generated with similar parameters except for fascicle radii and fascicle density. The left volume is generated with the parameters used in the simulations (Table I); the fascicle density (ρ_{fib}) is 0.4 fascicle/voxel^2, and the fascicle radii is 1.5 ± 0.5 voxel ($\mu_{r_{fib}} \pm \sigma_{r_{fib}}$). The middle volume is generated with thicker but fewer fascicles than the left volume; $\rho_{fib} = 0.03$ fascicle/voxel^2 and $\mu_{r_{fib}} \pm \sigma_{r_{fib}} = 6 \pm 2$ voxel. The volume to the right has largest but fewest fascicles; $\rho_{fib} = 0.1$ fascicle/voxel^2 and $\mu_{r_{fib}} \pm \sigma_{r_{fib}} = 12 \pm 2$ voxel. The geometry of the fascicles influences the accuracy and precision of strain tracking. The effect of modelling parameters on strain tracking performance could be investigated in future study.